

# Thermal and chemical evolution of the subarc mantle revealed by spinel-hosted melt inclusions in boninite from the Ogasawara (bonin) Archipelago, Japan

著者	Umino Susumu, Kitamura Keitaro, Kanayama Kyoko, Tamura Akihiro, Sakamoto Naoya, Ishizuka Osamu, Arai Shoji
journal or publication title	Geology
volume	43
number	2
page range	151-154
year	2015-02-01
URL	<a href="http://hdl.handle.net/2297/41329">http://hdl.handle.net/2297/41329</a>

doi: 10.1130/G36191.1

1 Thermal and chemical evolution of the subarc mantle revealed  
2 by spinel-hosted melt inclusions in boninite from the Ogasawara  
3 (Bonin) Archipelago

4 Susumu Umino<sup>1</sup>, Keitaro Kitamura<sup>1</sup>, Kyoko Kanayama<sup>1</sup>, Akihiro Tamura<sup>1</sup>, Naoya  
5 Sakamoto<sup>2</sup>, Osamu Ishizuka<sup>3</sup>, and Shoji Arai<sup>1</sup>

6 <sup>1</sup>*Division of Natural System, Kanazawa University, Kanazawa, Ishikawa 920-1192, Japan*

7 <sup>2</sup>*Creative Research Institution, Hokkaido University, Sapporo, Hokkaido 001-0021, Japan*

8 <sup>3</sup>*Geological Survey of Japan, Advanced Industrial Science and Technology, Tsukuba, Ibaraki*  
9 *305-8567, Japan*

10 **ABSTRACT**

11 Primitive melt inclusions in chrome spinel from the Ogasawara Archipelago comprise  
12 two discrete groups of high-SiO<sub>2</sub>, MgO (high-Si) and low-SiO<sub>2</sub>, MgO (low-Si) boninitic suites  
13 with ultra-depleted dish- and V-shaped, and less depleted flat rare earth element (REE) patterns.  
14 The most magnesian melt inclusions of each geochemical type were used to estimate the T-P  
15 conditions for primary boninites, that range from 1345°C-0.56 GPa to 1421°C-0.85 GPa for the  
16 48-46 Ma high-Si and low-Si boninites, and 1381°C-0.85 GPa for the 45 Ma low-Si boninite.  
17 The onset of the Pacific Slab subduction at 52 Ma forced upwelling of depleted mid-ocean ridge  
18 basalt mantle (DMM) to yield proto-arc basalt (PAB). With the rise of DMM, refractory  
19 harzburgite ascended without melting. At 48-46 Ma, introduction of slab fluids induced melting  
20 of the PAB residue and high-T harzburgite, resulted in the low-Si and high-Si boninites,  
21 respectively. Meanwhile, convection within the mantle wedge brought the less depleted residue

22 of PAB and DMM into the region fluxed by slab fluids, which melted to yield the less depleted  
23 low-Si boninite at 45 Ma, and fertile arc basalts, respectively.

## 24 **INTRODUCTION**

25         The Izu-Ogasawara (Bonin)-Mariana (or IBM) Arc has been a locus of intense study on  
26 oceanic arc evolution because it provides complete records of the volcanic arc development since  
27 the onset of the Pacific Plate subduction beneath the Philippine Sea Plate up to present (e.g.,  
28 Ishizuka et al., 2006, 2011). Along the entire IBM forearc MORB-like proto-arc basalt (PAB;  
29 Reagan et al., 2010) extruded at 52-48 Ma, followed by arc tholeiitic lavas on the Ogasawara  
30 Archipelago (Umino et al., 2009). The dissected tholeiitic rocks are overlain by 48-46 Ma highly  
31 depleted, high-silica boninite with minor low-silica boninite (Maruberiwan Formation), which  
32 became covered with less depleted, low-silica boninite associated with calc-alkalic magmas at 45  
33 Ma (Mikazukiyama Formation). By 44 Ma the volcanic front retreated westward and fertile arc  
34 magmas (Hahajima Island Group basalt, or HGB) superseded boninites (Kanayama et al., 2012;  
35 2014). This variation in magma geochemistry represents the thermo-chemical evolution of the  
36 mantle wedge during the establishment of the IBM arc.

37         Boninites potentially provide significant constraints on the P-T-X conditions of the  
38 varying mantle wedge because of their primitive compositions compatible with refractory upper  
39 mantle minerals (Umino, 1986; Crawford et al., 1989; Pearce et al., 1992; Kanayama et al.,  
40 2012). Specifically, melt inclusions in forsteritic olivine in boninite have been used for  
41 estimating primary magma compositions, based on which Tongan low-Si boninite was proposed  
42 to derive from hot mantle plumes with a mantle potential T (MPT) >1500°C (e.g., Sobolev &  
43 Danyushevsky, 1994; Sobolev and Chaussidon, 1996). However, most olivine-hosted melt  
44 inclusions suffered post-entrapment crystallization and diffusive reequilibration with the hosts,

45 which are irreversible by heating experiments (Kamenetsky et al., 2002; Kent, 2008). Especially  
46 Fe-loss is critical in estimating T-P conditions of primary boninite. Therefore, the original melt  
47 compositions upon entrapment were restored by raising FeO to the liquid line of descent, which  
48 was assumed to be equal to bulk compositions. Unfortunately, bulk compositions of porphyritic  
49 arc magmas like boninites mostly differ from the liquid compositions due to processes such as  
50 crystal accumulation and imperfect fractionation, and mixing of magmas.

51 In contrast, chrome spinel is an excellent container of primitive magmas because the  
52 trapped liquid compositions are little modified by crystallization of the host spinel due to limited  
53 Cr contents in melts (e.g., Shimizu et al., 2001). Furthermore, chrome spinel is resistant to  
54 deterioration compared to silicate minerals such as olivine, and chemically stable against low-  
55 grade metamorphic alteration. Chrome spinel is also eminently pressure-resistant as it may  
56 preserve ultra-high-pressure minerals (Yamamoto et al., 2009), so it is expected that chrome  
57 spinel may preserve primitive compositions of inclusions trapped under high temperatures and  
58 pressures.

59 This paper focuses on primitive melts preserved in chrome spinel, the earliest crystallized  
60 phase from boninite magmas in the Ogasawara Archipelago (Umino, 1986), to estimate the  
61 genetic conditions for primary magmas, and discusses the thermo-chemical evolution of the  
62 mantle wedge during the early stages of the IBM subduction zone development.

## 63 **SPINEL-HOSTED MELT INCLUSIONS**

### 64 **Mode of Occurrence of Melt Inclusions**

65 Boninites are widely exposed on the Mukojima and Chichijima islands, Ogasawara  
66 Archipelago, where chrome spinel samples were taken from the beach sand “Uguisu-zuna”,  
67 natural mineral concentrates of orthopyroxene and minor amounts of olivine, spinel +/-

68 clinopyroxene (Umino et al., 2009). Poorly developed river systems and generally consistent  
69 geochemistry and mineralogy of Uguisu-zuna and the surrounding geology support the view that  
70 those mineral concentrates were eroded from the nearby exposures and wave-sorted (Fig. DR-1).  
71 Melt inclusions are randomly distributed within spinel and have mainly oval or rounded  
72 triangular shapes constrained by crystallographic orientation of the host spinel. This indicates a  
73 primary origin for these inclusions trapped during the growth of the host spinel (Schiano, 2003).  
74 All melt inclusions in a single spinel crystal have the same texture and geochemical  
75 characteristics, indicating that these inclusions were trapped at the same time and experienced  
76 the same cooling history during ascent and quenching upon eruption.

77 Melt inclusions consist of glass with or without crystals. 21% of the inclusions examined  
78 are of entirely homogeneous glass (Figs. 1A, B, DR-2A, B) with or without shrinkage bubbles on  
79 the wall. The rest 79% carry daughter or captured crystals in addition to glass. Rare melt  
80 inclusions develop an outer zone of rapidly grown daughter pyroxene crystals surrounding a  
81 homogeneous glass pool in the core (Figs. 1C, DR-2C). However, both the outer zone and the  
82 core have identical bulk major element compositions (Fig. DR-3). About 27% of inclusions are  
83 “variolitic”, composed entirely of variolitic pyroxene crystals, interstitial glass and vesicles (Figs.  
84 1D, DR-2D). Both the “melt (glass)” dominant inclusions and the variolitic inclusions lack any  
85 compositional gradient through the inclusions and in the adjacent host spinel (Figs. 1, DR-2).  
86 The textural relationships and chemical homogeneity of these melt inclusions strongly suggest  
87 that the primary melt compositions at the time of entrapment are well preserved, in spite of the  
88 postentrapment crystallization in some inclusions. We therefore take the bulk compositions of  
89 these melt-dominant and variolitic inclusions as representative of quenched pristine melt  
90 compositions.

91

## 92 **Major and Trace Element Geochemistry**

93         The melt inclusions have 52-63 wt% SiO<sub>2</sub>, 7-23 wt% MgO and 0.01-0.25 wt% TiO<sub>2</sub> on  
94 an anhydrous basis (Fig. 2; Table DR-1). With few exceptions, almost all fit the category of  
95 boninite defined by the IUGS (SiO<sub>2</sub> >52 wt%, MgO >8 wt% and TiO<sub>2</sub> <0.5 wt%; Le Maitre,  
96 2002). Most inclusions form two roughly subparallel groups showing an inverse correlation of  
97 MgO and SiO<sub>2</sub>, which are generally consistent with fractionation paths of olivine followed by  
98 orthopyroxene (based on alphaMELTS by Smith and Asimow, 2005), combined with mixing of  
99 melts on the paths (Figs. 2A, DR-5). One group with higher MgO and SiO<sub>2</sub> falls within the field  
100 of high-silica boninite of Kanayama et al. (2012), but are more Mg-rich than the whole rocks at a  
101 given SiO<sub>2</sub> (“high-Si (boninitic) inclusions”, hereafter). The other group is somewhat scattered  
102 but plot between the high-Si inclusions and the bulk low-Si boninites, and are hence called “low-  
103 silica (low-Si) (boninitic) inclusions”. Almost all high-Si inclusions have low CaO (<8 wt%) and  
104 CaO/Al<sub>2</sub>O<sub>3</sub> ratios <0.8, characteristics of low-Ca boninite (Crawford, 1989). On the other hand,  
105 the low-Si inclusions have 6.5-12 wt% CaO and spread over the fields of both low-Ca and high-  
106 Ca boninites.

107         High-Si boninitic inclusions are severely depleted in REEs with chondrite-normalized  
108 patterns, which can be divided into dish-shaped (high-Si-D) and V-shaped (high-Si-V) at a  
109 Gd/Yb ratio of 0.7 (Fig. 2B). Dish-shaped REE patterns are identical to those of the bulk  
110 boninites in overall shape and abundance (Fig. DR-6). On the contrary, V-shaped REE patterns  
111 have never been found among the bulk rocks. High-Si-D and high-Si-V inclusions are enclosed  
112 in spinel with Cr/ (Cr + Al) of 0.85-0.91 and TiO<sub>2</sub> <0.12 wt% derived from the Maruberiwan

113 Formation. Although individual spinel grains have only a single type of inclusions, both high-Si-  
114 D and high-Si-V inclusions coexist in spinel samples from the same locality.

115 The low-Si boninitic inclusions are of two distinct types. One has less depleted, flat REE  
116 patterns with low  $Zr/Ti < 0.02$  (low-Si-F), and is only found in spinel derived from the  
117 Mikazukiyama Formation (Fig. 2C). Most of them possess a high-Ca boninitic affinity with  
118  $CaO/Al_2O_3$  ratios  $> 0.8$ . The other type, low-Si-D inclusions, is found in spinel from the  
119 Maruberiwan Formation and shows depleted dish-shaped REE patterns with variable  $Zr/Ti$  ratios  
120 (0.01-0.03), CaO (6-11 wt%) and  $CaO/Al_2O_3$  ratios (0.5-1). The host spinel of the low-Si  
121 inclusions has low  $Cr/(Cr + Al)$  of 0.72-0.87 and 0.04-0.24 wt%  $TiO_2$ .

122 The variolitic melt inclusions (Fig. 1D) tend to show lower  $H_2O$  contents ( $< 2.4$  wt%) and  
123  $H_2O/Ce$  ratios than the other inclusions (Fig. DR-4), suggesting water loss due to degassing. We  
124 therefore corrected water contents of variolitic samples by assuming their original  $H_2O/Ce$  ratios  
125 to be equal to the average  $H_2O/Ce$  ratios of undegassed samples of the same geochemical type.  
126 Because all low-Si-F inclusions exhibit a variolitic texture, the  $H_2O$  contents were restored based  
127 on the maximum  $H_2O/Ce$  ratio of the type, which gives the minimum  $H_2O$  estimates. The  
128 restored  $H_2O$  and  $H_2O/Ce$  ratios mostly range from 2 to 5 wt% and 9800-43200, respectively.

### 129 **Genetic Conditions of Primary Boninites**

130 If magma retains its primary composition, it should be multiply saturated with olivine and  
131 orthopyroxene at the temperature and pressure of segregation, which can be estimated by the  
132 combination of appropriate geothermobarometers. We applied the method of Putirka (2008)  
133 based on olivine-liquid equilibration (Putirka et al., 2007) and olivine-orthopyroxene-liquid  
134 equilibration (Putirka, 2008). Olivine-spinel equilibria suggests oxygen fugacity of boninite  
135 magma to be 0 to +1 in log unit above fayalite-magnetite-quartz (FMQ) buffer (Evans et al.,

136 2012), whereas  $\text{Fe}^{3+}/\text{Fe}^{2+}$  ratios of pillow margin glass estimated by XANES (Ishibashi et al.,  
137 2012) and sulfur speciation of melt inclusions in spinel determined by soft X-ray photoelectron  
138 spectroscopy (Shimizu et al., 2014) indicate  $f_{\text{O}_2}$  of  $\Delta\log(\text{FMQ}) = +1 \sim +2$  for the Ogasawara  
139 boninite. We therefore assumed  $f_{\text{O}_2}$  of  $\Delta\log(\text{FMQ}) = 1 \pm 1$  for the T-P estimates.  $\text{CO}_2$   
140 concentrations of boninitic melt inclusions in chrome spinel from the Ogasawara Archipelago are  
141 very low (<50 ppm; Shimizu and Shimizu, 2013) and hence  $\text{H}_2\text{O}$  is considered as the only  
142 volatile species. The compositions of primary boninite magmas are assumed to be those of the  
143 most magnesian melt inclusions among the four geochemical types described above, i.e. high-Si-  
144 D, high-Si-V, low-Si-D and low-Si-F melt inclusions (Table DR-1). The estimated equilibration  
145 T and P are 1343-47°C at 0.54-0.59 GPa for the low-Si-D boninite, and 1415-28°C at 0.74-0.96  
146 GPa for the high-Si-D and high-Si-V boninites (Fig. 3). The genetic T-P of 1378-1384°C and  
147 0.81-0.88 GPa for the low-Si-F boninite are considered to be the maximum estimates, because its  
148  $\text{H}_2\text{O}$  content is the minimum estimate.

## 149 **DISCUSSION**

150 There is a general consensus that boninitic magmas derive from severely depleted source  
151 mantle which experiences flux melting by introduction of hydrous fluids (or melts) liberated  
152 from a descending slab (e.g. Pearce et al. 1992; Bédard, 1999; Kanayama et al., 2012). These  
153 studies ascribed high Zr/Ti ratios of high-Si boninites to contribution of slab melt under  
154 amphibolite facies. The degree of depletion of the source mantle can be assessed by  
155 concentrations of heavy REEs such as Yb, which are predominantly immobile through slab  
156 dehydration and sediment partial melting. Figure 4 shows Yb-Zr/Ti variations modeled by 5%  
157 and 20% batch partial melts of residual DMM (Workman and Hart, 2005) after extraction of 0%  
158 to 20% fractional melts, mixed with 5% batch partial melt of amphibolitic slab (based on altered



159 oceanic basalt at Site 1149; Kelley et al., 2003). The model indicates that Yb concentrations are  
160 more sensitive to the degree of source depletion than that of batch melting. Both the PAB and the  
161 HGB have the least depleted source mantle and little contribution from slab melts. Irrespective to  
162 the degree of melting of the residual DMM, the highest Yb and the least Zr/Ti for the 45 Ma low-  
163 Si-F inclusions indicate less than 11-16% source depletion and contribution of 8-15% slab melt,  
164 smallest among all melt inclusions. The 48-46 Ma high-Si-D and high-Si-V inclusions have the  
165 least Yb and the highest Zr/Ti, indicating the largest source depletion up to 19-24% and mixing  
166 of 10-20% slab melt. Although the 48-46 Ma low-Si-D inclusions are similarly low in Yb, the  
167 model suggests slightly lower depletion of 17-20%.

168         Subsidence of the old, dense Pacific Plate caused forearc spreading and decompression  
169 melting of DMM-like asthenosphere to form MORB-like PAB magma for the first few million  
170 years after the subduction initiated (Ishizuka et al., 2011; Kanayama et al., 2012). If the PAB  
171 source had a MPT of  $\sim 1410^{\circ}\text{C}$ , which is slightly above the present suboceanic ambient mantle  
172 (Herzberg et al., 2007), the residue would become  $\sim 1345^{\circ}\text{C}$  at 0.5 GPa, coincident with the T-P  
173 conditions for the 48-46 Ma low-Si-D boninite magma, supporting the remelting of the PAB  
174 residue (Fig. 3). However, it is incompatible with the coexistence of extremely hot ( $>1400^{\circ}\text{C}$  at  
175 0.8 GPa), severely depleted source mantle of the high-Si boninite magmas. If, as the plume-  
176 origin model of boninite suggests, the pre-boninite decompression melting of the DMM was  
177 solely responsible for the extreme depletion of the boninite source, it should have ascended from  
178 the depth of 3.5 GPa with a MPT of  $1500^{\circ}\text{C}$ . The ascent of such high-T peridotite to  $<1$  GPa  
179 should cause extensive decompression melting to produce picritic magmas, which have never  
180 been found among the pre-boninite PAB. This indicates that the depleted proto-boninite source  
181 already existed below the DMM-like PAB source before the subduction began. This is supported

182 by the unradiogenic Os isotopic composition of harzburgite drilled in the Izu Forearc, which  
183 experienced melt extraction in Proterozoic age and became the source for the IBM boninite  
184 magmas (Parkinson et al., 1998; Suzuki et al., 2011). With the DMM asthenosphere, the  
185 refractory harzburgitic source ascended along the adiabatic decompression path without melting,  
186 resulted in the high temperatures of the high-Si boninites (Fig. 3). Considering 1380°C and 0.8  
187 GPa are the maximum estimates for the low-Si-F boninite genesis, it would be close to the  
188 adiabatic melting path of the PAB source. Compared to the low-Si-D boninite, the low-Si-F  
189 boninite has the higher T-P and less depleted source, suggesting its derivation from the periphery  
190 of the asthenospheric upwelling, which suffered lower degrees of melting and ascended off the  
191 forearc spreading axis. By 45 Ma, convection in the wedge mantle driven by drag force of the  
192 subducting slab brought the less depleted low-Si-F boninite source and DMM-like asthenosphere  
193 into the region fluxed by slab fluids, which melted to generate the low-Si-F boninite magma, and  
194 then arc tholeiitic and calc-alkalic magmas on the Hahajima Island Group and the western scarps  
195 of the Ogasawara Ridge.

## 196 **ACKNOWLEDGMENTS**

197 This study was supported by the Geological Survey of Japan and MEXT Special  
198 Budget Project No. 812000009 to S.A. and No. 25287133 to O.I. We thank N. Yurimoto  
199 (Hokkaido University) for the usage of SIMS, and N. Chatterjee, A.J. Arculus and F.  
200 Sorbadere for their critical reviews.

## 201 **REFERENCES CITED**

202

- 203 Bédard, J.H., 1999, Petrogenesis of boninites from the Betts Cove Ophiolite, Newfoundland,  
204 Canada: Identification of subducted source components: *Journal of Petrology*, v. 40,  
205 p. 1853–1889, doi:10.1093/petroj/40.12.1853.
- 206 Crawford, A.J., Falloon, T.J., and Green, D.H., 1989, Classification, petrogenesis and tectonic  
207 setting of boninites, *in* Crawford, A.J., ed., *Boninites and Related Rocks*: London, Unwyn-  
208 Hyman Ltd., p. 1–49.
- 209 Evans, K.A., Elburg, M.A., and Kamenetsky, V.S., 2012, Oxydation state of subarc mantle:  
210 *Geology*, v. 40, 783 - 786.
- 211 Grove, T.L., Chatterjee, N., Parman, S.W., and Médard, E., 2006, The influence of H<sub>2</sub>O on  
212 mantle wedge melting: *Earth and Planetary Science Letters*, v. 249, p. 74–89,  
213 doi:10.1016/j.epsl.2006.06.043.
- 214 Grove, T.L., Till, C.B., Lev, E., Chatterjee, N., and Méard, E., 2009, Kinematic variables and  
215 water transport control the formation and location of arc volcanoes: *Nature*, v. 459, p. 694–  
216 697, doi:10.1038/nature08044.
- 217 Herzberg, C., Asimow, P.D., Arndt, N., Niu Y., Leshner, C.M., Fitton, J.G., Cheadle, M.J., and  
218 Saunders, A.D., 2007. Temperatures in ambient mantle and plumes: Constraints from basalts,  
219 picrite, and komatiites: *Geochemistry, Geophysics, Geosystems*, v. 8, Q02006, doi:  
220 10.1029/2006GC001390.
- 221 Herzberg, C., and Gazel, E., 2009, Petrological evidence for secular cooling in mantle plumes:  
222 *Nature*, v. 458, p. 619–622, doi:10.1038/nature07857.
- 223 Ishibashi, H., Odake, S., Kanayama, K., Hamada, M., and Kagi, H., 2013. The redox states of  
224 basaltic and boninitic magmas erupted at the early stage of the Bonin arc formation; Fe-K  
225 edge XANES study: IAVCEI Scientific Meeting 2013, Kagoshima.

- 226 Ishizuka, O., Kimura, J., Li, Y.B., Stern, R.J., Reagan, M.K., Taylor, R.N., Ohara, Y., Bloomer,  
227 S.H., Ishii, T., Hargrove III, U.S., and Haraguchi, S., 2006, Early stages in the evolution of  
228 Izu-Bonin arc volcanism: New age, chemical, and isotopic constraints: *Earth and Planetary  
229 Science Letters*, v. 250, p. 385–401, doi:10.1016/j.epsl.2006.08.007.
- 230 Ishizuka, O., Tani, K., Reagan, M.K., Kanayama, K., Umino, S., Harigane, Y., Sakamoto, I.,  
231 Miyajima, Y., Yuasa, M., and Dunkley, D.J., 2011, The timescales of subduction initiation  
232 and subsequent evolution of an oceanic island arc: *Earth and Planetary Science Letters*,  
233 v. 306, p. 229–240, doi:10.1016/j.epsl.2011.04.006.
- 234 Kamenetsky, V.S., Sobolev, A.V., Eggins, S.M., Crawford, A.J., and Arculus, R.J., 2002,  
235 Olivine-enriched melt inclusions in chromites from low-Ca boninites, Cape Vogel, Papua  
236 New Guinea: evidence for ultramafic primary magma, refractory mantle source and enriched  
237 components: *Chemical Geology*, v. 183, p. 287–303.
- 238 Kanayama, K., Umino, S., and Ishizuka, O., 2012, Eocene volcanism during the incipient stage  
239 of Izu–Ogasawara Arc: *Geology and petrology of the Mukojima Island Group, the  
240 Ogasawara Islands: The Island Arc*, v. 21, p. 288–316, doi:10.1111/iar.12000.
- 241 Kanayama, K., Umino, S., and Ishizuka, O., 2014, Shallow submarine volcano group in the early  
242 stage of island arc development: *Geology and petrology of small islands south off Hahajima  
243 main island, the Ogasawara Islands: Journal of Asian Earth Sciences*, v. 85, p. 1–25,  
244 doi:10.1016/j.jseaes.2014.01.012.
- 245 Kelley, K.A., Plank, T., Ludden, J., and Staudigel, H., 2003, Composition of altered oceanic  
246 crust at ODP sites 801 and 1149: *Geochemistry Geophysics Geosystems*, v. 4,  
247 doi:10.1029/2002GC000435.

- 248 Kent, A.J.R., 2008, Melt inclusions in basaltic and related volcanic rocks, *in* Putirka, K.D., and  
249 Teply, F.J. III, eds., *Reviews in Mineralogy and Geochemistry* 69, p. 273–331.
- 250 Le Maitre, R.W., ed., 2002, *Igneous Rocks, A Classification And Glossary Of Terms:*  
251 *Recommendations Of The International Union Of Geological Sciences Subcommission On*  
252 *The Systematics Of Igneous Rocks:* Cambridge, Cambridge University Press, p. 236.
- 253 Parkinson, I.J., Hawkesworth, C.J., and Cohen, A.S., 1998, Ancient mantle in a modern arc:  
254 Osmium isotopes in Izu-Bonin-Mariana forearc peridotites: *Science*, v. 281, p. 2011–2013,  
255 doi:10.1126/science.281.5385.2011.
- 256 Pearce, J.A., van der Laan, S.R., Arculus, R.J., Murton, B.J., Ishii, T., Peate, D.W., and  
257 Parkinson, I.J., 1992, Boninite and harzburgite from Leg 125 (Bonin-Mariana forearc): a  
258 case study of magma genesis during the initial stages of subduction, *in* Fryer, P., Pearce,  
259 J.A., Stokking, L.B., et al., eds., *Proceedings of Ocean Drilling Program, Scientific Results,*  
260 *volume 125:* College Station, TX, Ocean Drilling Program, p. 623–659.
- 261 Putirka, K., 2008, Thermometers and Barometers for Volcanic Systems, *in* Putirka, K.D., and  
262 Teply, F.J. III, eds., *Reviews in Mineralogy and Geochemistry*, v. 69, p. 61–120.
- 263 Putirka, K.D., Perfit, M., Ryerson, F.J., and Jackson, M.G., 2007, Ambient and excess mantle  
264 temperatures, olivine thermometry, and active vs. passive upwelling: *Chemical Geology*,  
265 v. 241, p. 177–206, doi:10.1016/j.chemgeo.2007.01.014.
- 266 Reagan, M.K., Ishizuka, O., Stern, R.J., Kelley, K.A., Ohara, Y., Blichert-Toft, J., Bloomer, S.H.,  
267 Cash, J., Fryer, P., Hanan, B.B., Hickey-Vargas, R., Ishii, T., Kimura, J., Peate, D.W., Rowe,  
268 M.C., and Woods, M., 2010, Fore-arc basalts and subduction initiation in the Izu-Bonin-  
269 Mariana system: *Geochemistry Geophysics Geosystems*, v. 11, p. Q03X12,  
270 doi:10.1029/2009GC002871.

- 271 Schiano, P., 2003, Primitive mantle magmas recorded as silicate melt inclusions in igneous  
272 minerals: *Earth-Science Reviews*, v. 63, p. 121–144, doi:10.1016/S0012-8252(03)00034-5.
- 273 Shimizu, K., and Shimizu, N., 2013, Volatile behavior in an immature subduction zone inferred  
274 from boninitic melt inclusions in Cr-spinel: *Goldschmidt 2013, Florence, Abstracts*, 07c.
- 275 Shimizu, K., Komiya, T., Hirose, K., Shimizu, N., and Maruyama, S., 2001, Cr-spinel, an  
276 excellent micro-container for retaining primitive melts — implications for a hydrous plume  
277 origin for komatiites: *Earth and Planetary Science Letters*, v. 189, p. 177–188,  
278 doi:10.1016/S0012-821X(01)00359-4.
- 279 Shimizu, K., Kashiwabara, T., and Tamenori, Y., 2014, Oxidation state of magmas at an  
280 immature subduction zone-inferred from sulfur speciation of boninitic and tholeiitic melt  
281 inclusions: *Sacramento, Goldschmidt 2014, Abstracts*, 08d.
- 282 Smith, P.M., and Asimow, P.D., 2005, *Adiabat\_1ph*: A new public front-end to the MELTS,  
283 *pMELTS*, and *pHMELTS* models: *Geochemistry Geophysics Geosystems*, v. 6, p. Q02004,  
284 doi:10.1029/2004GC000816.
- 285 Sobolev, A.V., and Chaussidon, M., 1996, H<sub>2</sub>O concentrations in primary melts from supra-  
286 subduction zones and mid-ocean ridges: Implications for H<sub>2</sub>O storage and recycling in the  
287 mantle: *Earth and Planetary Science Letters*, v. 137, p. 45–55, doi:10.1016/0012-  
288 821X(95)00203-O.
- 289 Sobolev, A.V., and Danyushevsky, L.V., 1994, Petrology and Geochemistry of Boninites from  
290 the North Termination of the Tonga Trench: Constraints on the Generation Conditions of  
291 Primary High-Ca Boninite Magmas: *Journal of Petrology*, v. 35, p. 1183–1211,  
292 doi:10.1093/petrology/35.5.1183.

- 293 Suzuki, K., Senda, R., and Shimizu, K., 2011, Osmium behavior in a subduction system  
294 elucidated from chromian spinel in Bonin Island beach sands: *Geology*, v. 39, p. 999–1002,  
295 doi:10.1130/G32044.1.
- 296 Taylor, R.N., Nesbitt, R.W., Vidal, P., Harmon, R.S., Auvray, B., and Croudace, I.W., 1994,  
297 Mineralogy, chemistry, and genesis of the Boninite series volcanics, Chichijima, Bonin  
298 Islands, Japan: *Journal of Petrology*, v. 35, p. 577 - 618.
- 299 Umino, S., 1986, Magma mixing in boninite sequence of Chichijima, Bonin Islands: *Journal of*  
300 *Volcanology and Geothermal Research*, v. 29, p. 125–157, doi:10.1016/0377-  
301 0273(86)90042-9.
- 302 Umino, S., Nakano, S., Ishizuka, O., and Komazawa, M., 2009, Geological Map of Japan  
303 1:200,000, Ogasawara Shotô (in Japanese with English abstract): Geological Survey of  
304 Japan, AIST.
- 305 Workman, R.K., and Hart, S.T., 2005, Major and trace element composition of the depleted  
306 MORB mantle (DMM): *Earth and Planetary Science Letters*, v. 231, p. 53–72,  
307 doi:10.1016/j.epsl.2004.12.005.
- 308 Yamamoto, S., Komiya, T., Hirose, K., and Maruyama, S., 2009, Coesite and clinopyroxene  
309 exsolution lamellae in chromites: In-situ ultrahigh-pressure evidence from podiform  
310 chromitites in the Luobusa ophiolite, southern Tibet: *Lithos*, v. 109, p. 314–322,  
311 doi:10.1016/j.lithos.2008.05.003.

## 312 **FIGURE CAPTIONS**

313 Figure 1. Representative COMPO images (left) and electron microprobe analyzer (EMPA)  
314 elemental maps showing textures, and Fe and Mg distributions respectively of melt inclusions

315 and the host chrome spinel. Note the absence of Fe-rich and Mg-poor halos in the spinel host  
316 adjacent to the melt inclusions, confirming the absence of diffusive Fe-loss from the melt.  
317 Figure 2. Boninitic melt inclusions (circles and squares) compared with bulk boninites (crosses)  
318 of the 48-46 Ma Maruberiwan (Mb) and 45 Ma Mikazukiyama (Mk) Formations from  
319 Ogasawara. Examples of fractionation paths for primary boninites (solid and broken lines) are  
320 shown at 0.2 GPa and  $fO_2$  of 0.5 log unit above fayalite-magnetite-quartz (FMQ) buffer using  
321 alphaMELTS (A), chondrite-normalized REE patterns of high-Si-D and high-Si-V (B) and low-  
322 Si-D and low-Si-F (C) inclusions. Broken lines encircle the bulk boninites. See Fig. DR-5 for  
323 further explanation.

324 Figure 3. T-P estimates of multiple saturation for the primary boninite magmas. The ranges of T-  
325 P estimates denote  $1\sigma$  of  $H_2O$  and  $fO_2$  of  $\Delta\log(FMQ) = 1\pm 1$ . Note that varying  $fO_2$  by 2 in log  
326 unit brings a little difference in T-P estimates, but increase in  $H_2O$  content by 1 wt% reduces the  
327 estimated T and P by  $34^\circ C$  and 0.17 GPa, respectively. Adiabatic melting paths are after  
328 Herzberg and Gazel (2009). The broken arrow is that for the DMM asthenosphere with  $MPT =$   
329  $1410^\circ C$ . The solid arrow is an adiabatic decompression path of the harzburgite source for the  
330 high-Si boninite, calculated using  $dT/dP = 13.3^\circ C/GPa$  (Putirka et al., 2007). The harzburgite  
331 solidus is based on the residual DMM after 20% fractional melting by alphaMELTS.

332 Figure 4. Yb vs Zr/Ti of boninitic melt inclusions compared with pre-boninite PAB, bulk  
333 boninites and post-boninite HGB. Symbols are the same as in Fig. 2. The Yb-Zr/Ti relationships  
334 is modeled by mixing of 5% (gray) and 20% (black) batch partial melts of residual DMM after  
335 extraction of 0-20% fractional melts (denoted such as "10%"), and 5% batch partial melt of  
336 amphibolitic slab (based on altered oceanic basalt at Site 1149; Kelley et al., 2003) with a  
337 proportion of clinopyroxene: amphibole:plagioclase = 7:88:5 (Taylor et al., 1994). Numbers on



338 the broken lines (“70:30”, etc.) are the proportions of peridotite melt:slab melt. Increase in slab  
339 melting up to 15% does not change the model results.

340 <sup>1</sup>GSA Data Repository item 2014xxx, Boninitic melt inclusions in chrome spinel from the  
341 Ogasawara Archipelago, is available online at [www.geosociety.org/pubs/ft2014.htm](http://www.geosociety.org/pubs/ft2014.htm), or on  
342 request from [editing@geosociety.org](mailto:editing@geosociety.org) or Documents Secretary, GSA, P.O. Box 9140, Boulder,  
343 CO 80301, USA.

Fig. 1

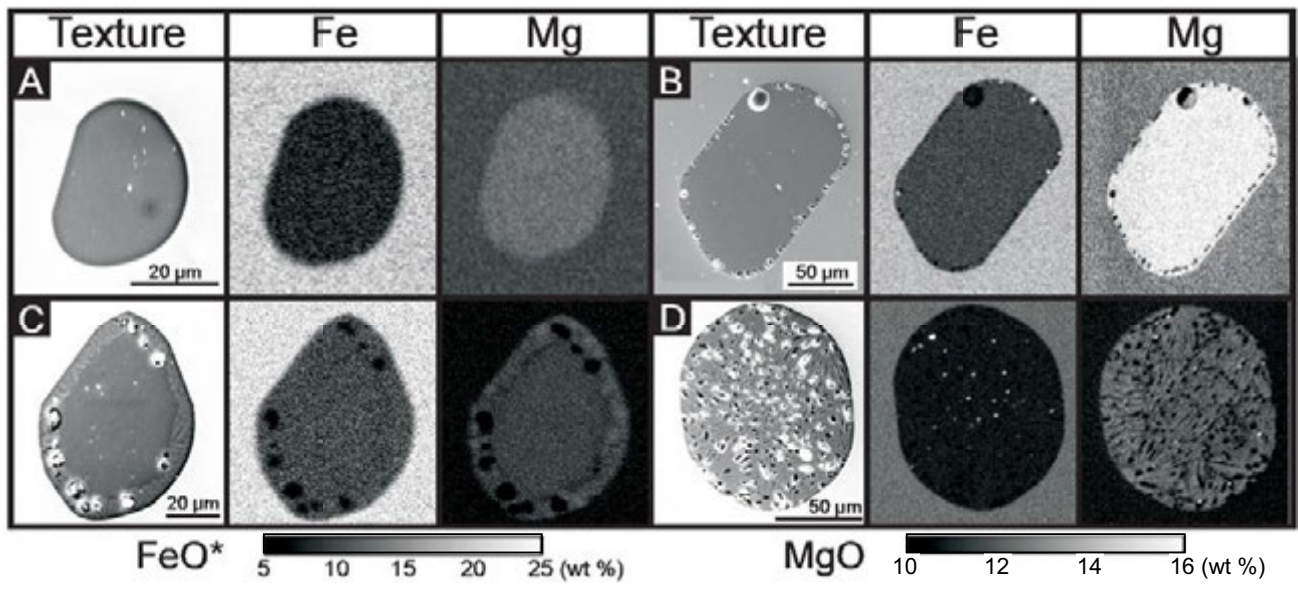


Fig. 2

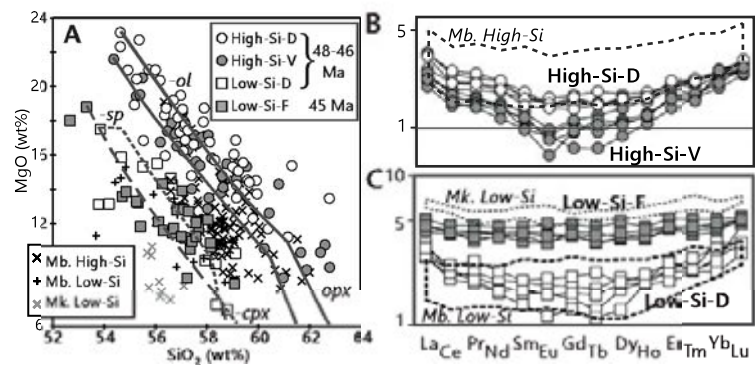


Fig. 3

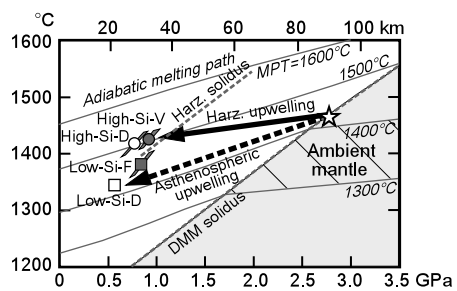
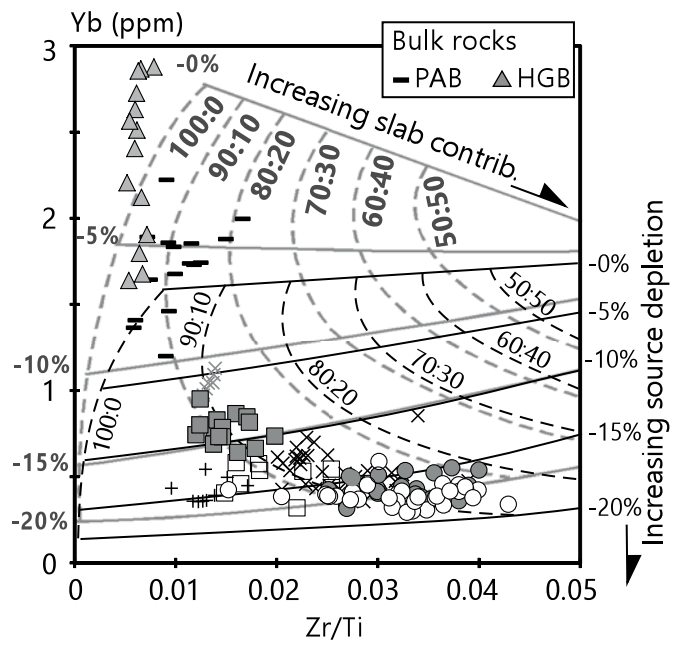


Fig. 4



**BONINITIC MELT INCLUSIONS IN CHROME SPINEL FROM THE OGASAWARA  
ARCHIPELAGO**

**DATA REPOSITORY** for “Thermal and chemical evolution of the subarc mantle revealed by spinel-hosted melt inclusions in boninite from the Ogasawara (Bonin) Archipelago” by Susumu Umino, Keitaro Kitamura, Kyoko Kanayama, Akihiro Tamura, Naoya Sakamoto, Osamu Ishizuka, and Shoji Arai.

**Analytical methods and procedures**

Chrome spinels were handpicked under binocular after cleaning and sieving the sand samples with pure water. Spinel crystals embedded in epoxy resin on a slide glass were ground and polished to expose the core of crystals with melt inclusions, which were utilized for major and trace element analyses, including H<sub>2</sub>O (Table DR-1).

Major elements of glass and minerals were analyzed by a JEOL JXA-8800 electron probe microanalyzer (EPMA) at Kanazawa University. The accelerating voltage was 15 kV and the specimen current was 12 nA. Analyses of glass followed the procedures of Noguchi *et al.* (2004) using broad beam diameters <30 μm. The corrections were made according to ZAF method. Relative errors (1σ) of melt inclusion analyses are better than 0.4% for SiO<sub>2</sub>, 11.3% for TiO<sub>2</sub>, 1.3% for Al<sub>2</sub>O<sub>3</sub>, 3.0% for FeO, 23.3% for MnO, 1.2% for MgO, 1.7% for CaO, 7.8% for Na<sub>2</sub>O, 7.9% for K<sub>2</sub>O and 6.7% for Cr<sub>2</sub>O<sub>3</sub>.

Trace element compositions (REEs, V, Cr, Co, Ni, Li, B, Sc, Rb, Sr, Y, Zr, Nb, Cs, Ba, Hf, Ta, Pb, Th and U) of glass were analyzed by laser ablation (193 nm ArF excimer: MicroLas GeoLas Q-plus) inductively coupled plasma mass spectrometry (Agilent 7500s) (LA-ICP-MS) at Kanazawa University (Morishita *et al.*, 2005a, b). Each analysis was performed by ablating spots of 30 or 40 μm in diameter at 5 Hz with energy density of 8 J/cm<sup>2</sup> per pulse. Signal integration times were 50 seconds for a gas background interval and 50 seconds for an ablation interval. BCR-2G (USGS glass reference material) was used as the primary calibration standard and its element concentration values are selected from the GeoReM database (see Jochum and Nohl., 2008). Repeated analyses of NIST 610, NIST612 and BIR show that reproducibility is better than ±11% (1 σ)

Umino et al.

except B, Cs, Ta and U (Table DR-2). Data reduction was facilitated using  $^{29}\text{Si}$  as internal standards for glass, based on  $\text{SiO}_2$  contents obtained by EPMA analysis, and followed a protocol essentially identical to that outlined by Longerich et al. (1996). Details of the analytical method and data quality for the LA-ICP-MS system at Kanazawa University are described in Morishita et al. (2005a, b) and Ichiyama et al. (2013).

$\text{H}_2\text{O}$  concentrations in glass of melt inclusions were determined by using a Secondary Ion Mass Spectrometry (SIMS) Cameca IMS-6F of the Creative Research Institution, Hokkaido University. Analytical procedures followed Miyagi and Yurimoto (1995) using natural hornblende with 1.66 wt%  $\text{H}_2\text{O}$  as a standard. Water contents (in wt%) were determined by comparing  $^1\text{H}/^{30}\text{Si}$  ratios of unknown samples with averages of those of the standard hornblende measured on the same day.

### **Water content**

$\text{H}_2\text{O}$  contents vary from 1 to 5 wt% and  $\text{H}_2\text{O}/\text{Ce}$  ratios from 2000 to 43200. Interstitial glass in melt inclusions consisting mainly of variolitic pyroxene crystals and vesicles (Fig. 1D) tends to show lower  $\text{H}_2\text{O}$  concentrations (<2.4 wt%). These glass inclusions have consistently lower  $\text{H}_2\text{O}/\text{Ce}$  ratios compared to glass in melt inclusions comprising pure glass and a few shrinkage vesicles of the same geochemical type (Fig. DR-4).  $\text{H}_2\text{O}$  and Ce do not fractionate during partial melting of the source mantle and fractional crystallization of magmas due to their similar partition coefficients between melt and relevant mineral phases (Michael, 1995; Hauri et al., 2006), and hence melt inclusions of the same geochemical type are expected to have similar  $\text{H}_2\text{O}/\text{Ce}$  ratios. Thus, the coincidence of the variolitic texture and the lower  $\text{H}_2\text{O}$  contents and  $\text{H}_2\text{O}/\text{Ce}$  ratios compared to those of pure glass inclusions of the same geochemical type suggests that the variolitic melt inclusions experienced degassing and partially lost their original water during ascent to the surface. We therefore have corrected water contents of degassed samples and estimated the original water contents based on Ce contents, by assuming the original  $\text{H}_2\text{O}/\text{Ce}$  ratios of the degassed samples to be equal to the average  $\text{H}_2\text{O}/\text{Ce}$  ratio of undegassed samples of the same geochemical type. Because all low-Si-F (flat chondrite-normalized REE pattern) inclusions show a variolitic texture with low  $\text{H}_2\text{O}/\text{Ce}$  ratios, the original  $\text{H}_2\text{O}/\text{Ce}$  ratio of the type was assumed to be 9800, the maximum ratio among Type F inclusions observed. This gives the minimum

## Data Repository

estimates of the original H<sub>2</sub>O contents for low-Si-F inclusions. The restored H<sub>2</sub>O contents range from 1 to 6 wt% with restored H<sub>2</sub>O/Ce ratios varying from 9800 to 43200.

### **Procedure of T-P estimate of olivine-orthopyroxene multiple saturation**

T-P estimates for the primary boninitic magmas to be multiply saturated with olivine and orthopyroxene were determined by solving simultaneously the olivine-liquid geothermobarometry (equation (4) of Putirka et al., 2007) and olivine-orthopyroxene-liquid geothermobarometry (equation (42) of Putirka, 2008), following the procedure described in Putirka (2008). Major element compositions including Fe<sub>2</sub>O<sub>3</sub>, and H<sub>2</sub>O contents are used as input. First, (1) The Fe<sup>3+</sup>/Fe<sup>2+</sup> ratio at prescribed f<sub>O2</sub> (here  $\Delta\log(\text{FMQ}) = 0$  to +2) and the liquidus temperature is determined by using alphaMELTS (Smith and Asimow, 2005) at initial guess of pressure. (2) T and P obtained from the geothermobarometry are then used to calculate Fe<sup>3+</sup>/Fe<sup>2+</sup> ratio at prescribed f<sub>O2</sub> by alphaMELTS. (1) and (2) are repeated iteratively until T, P, and Fe<sup>3+</sup>/Fe<sup>2+</sup> ratio become stable within 0.5%. Varying f<sub>O2</sub> by 2 in log unit brings a little difference in T-P estimates compared to the uncertainty inherited from the geothermobarometry, while increase in H<sub>2</sub>O content by 1 wt% reduces the estimated T and P by 34°C and 0.17 GPa, respectively.

## **REFERENCES**

- Falloon, T.J., and Danyushevsky, L.V., 2000, Melting of refractory mantle at 1.5, 2 and 2.5 GPa under anhydrous and H<sub>2</sub>O-saturated conditions: Implications for the petrogenesis of high-Ca boninites and the influence of subduction components on mantle melting: *Journal of Petrology*, v. 41, p. 257–283.
- Hauri, E.H., Gaetani, G.A., and Green, T.H., 2006, Partitioning of water during melting of the Earth's upper mantle at H<sub>2</sub>O-undersaturated conditions: *Earth and Planetary Science Letters*, v. 248, 715–734.
- Ichiyama, Y., Morishita, T., Tamura, A., and Arai, S., 2013, Petrology of peridotite xenolith-bearing basaltic to andesitic lavas from the Shiribeshi Seamount, off northwestern Hokkaido, the Sea of Japan: *Journal of Asian Earth Sciences*, v. 76, p. 48–58.



Umino et al.

- Jochum, K. P., and Nohl, U., 2008, Reference materials in geochemistry and environmental research and the GeoReM database: *Chemical Geology*, v. 253, p. 50–53.
- Longerich, H.P., Jackson, S.E. and Gunther, D., 1996, Laser ablation inductively coupled plasma mass spectrometric transient signal data acquisition and analyte concentration calculation: *Journal of Analytical Atomic Spectrometry*, v. 11, p. 899–904.
- Michael, P., 1995, Regionally distinctive sources of depleted MORB: Evidence from trace elements and H<sub>2</sub>O: *Earth and Planetary Science Letters*, v. 131, p. 301–320.
- Miyagi, I., and Yurimoto, H., 1995, Water content of melt inclusions in phenocrysts using Secondary Ion Mass Spectrometer: *Bulletin of Volcanological Society of Japan*, v. 40, p. 349–355.
- Morishita, T., Ishida, Y., and Arai, S., 2005a, Simultaneous determination of multiple trace element compositions in thin (<30 µm) layers of BCR-2G by 193 nm ArF excimer laser ablation-ICP-MS: implications for matrix effect and elemental fractionation on quantitative analysis: *Geochemical Journal*, v. 39, p. 327–40.
- Morishita, T., Ishida, Y., Arai, S., and Shirasaka, M., 2005b, Determination of multiple trace element compositions in thin (30 µm) layers of NIST SRM 614 and 616 using laser ablation-inductively coupled plasma-mass spectrometry (LA-ICP-MS): *Geostandards and Geoanalytical Research*, v. 29, p. 107-122.
- Noguchi, S., Morishita, T., and Toramaru, A., 2004, Corrections for Na-loss on micro-analysis of glasses by electron probe X-ray micro analyzer (in Japanese with English abstract): *Japanese Magazine of Mineralogical and Petrological Sciences*, v. 33, p. 85–95.
- Smith, P.M., and Asimow, P.D., 2005, *Adiabat\_1ph*: A new public front-end to the MELTS, pMELTS, and pHMELTS models: *Geochemistry, Geophysics, Geosystems*, v. 6, Q02004, doi:10.1029/2004GC000816.

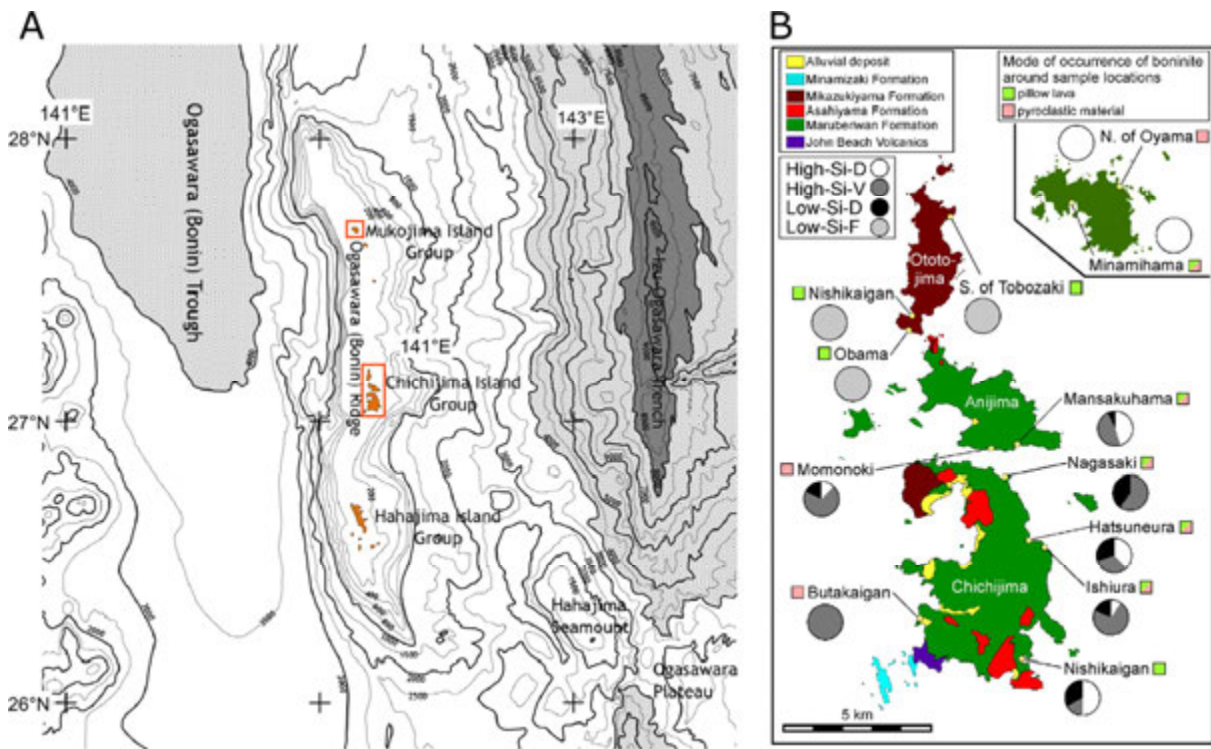


Figure DR-1. Locations of the Ogasawara Archipelago (A) and samples of chrome spinel together with the mode of occurrence of the host rocks and geochemical types (B).

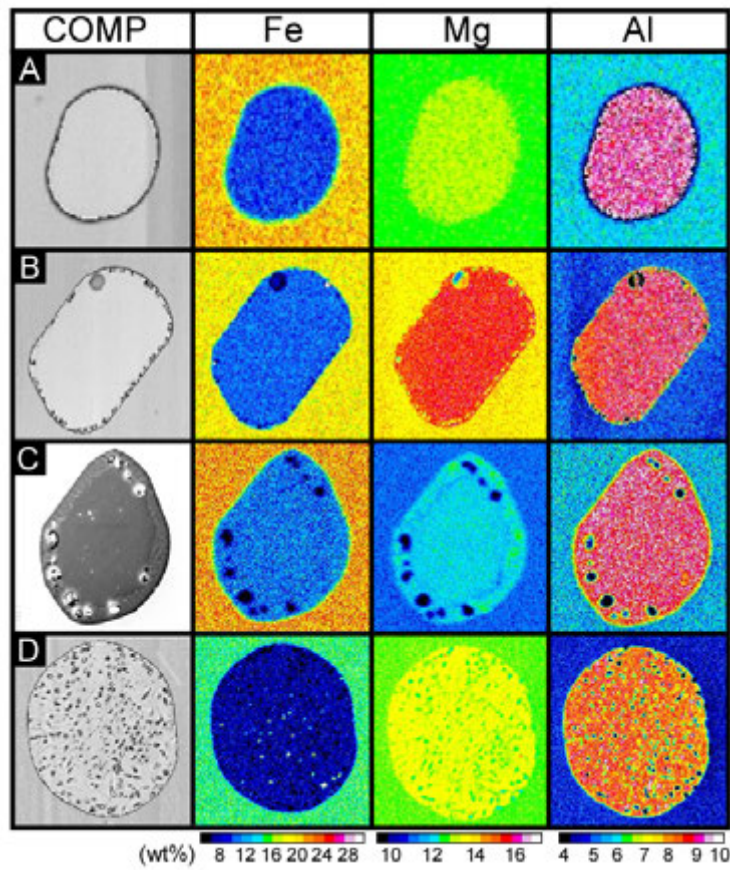


Figure DR-2. SEM (COMPO) images (left) and pseudo-colored EMPA maps (right) of Fe, Mg, and Al of melt inclusions and the host chrome spinel shown in Figure 1. Note the absence of Fe-rich and Mg-poor halos in the spinel host adjacent to the melt inclusions, confirming the absence of diffusive Fe-loss from the melt.

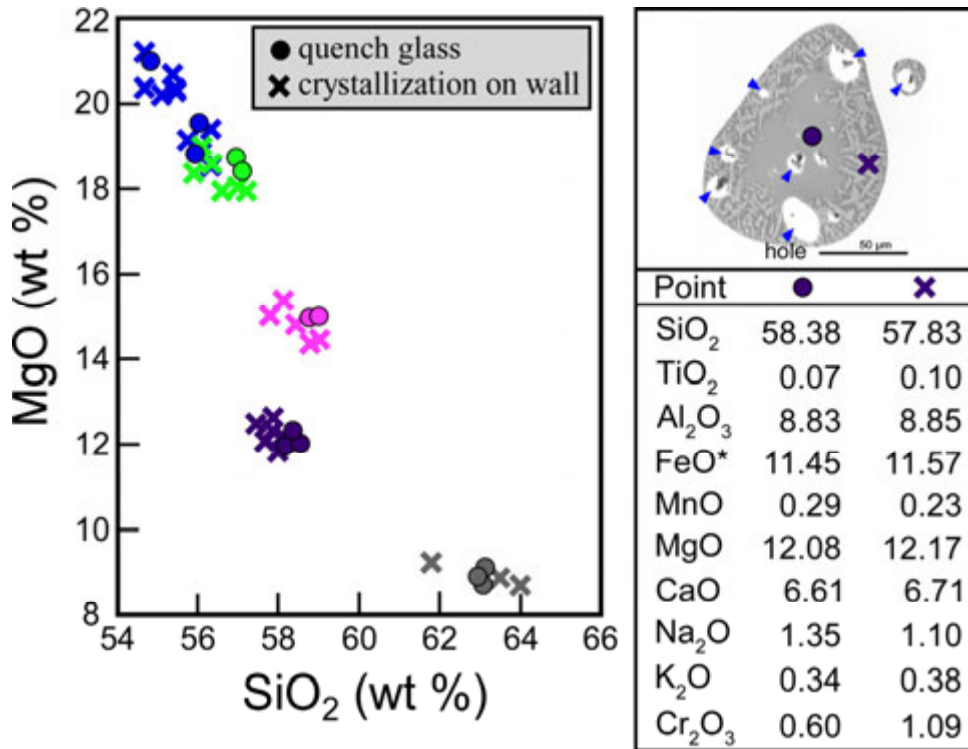


Figure DR-3. Analyses of melt inclusions (left) composed of the central glass pool (dots) surrounded by an outer zone with quench crystals and interstitial glass (crosses). A SEM image (upper right) shows dark grey glass rimmed by a zone with light grey quench crystals. Bright spots are holes (blue arrows) due to edge effect. Symbols with the same colors are analyses of the same inclusions. Note that both outer zones and central glass pools have identical bulk compositions, indicating that crystallization of the outer zone did not affect the composition of the remaining melt in the core.

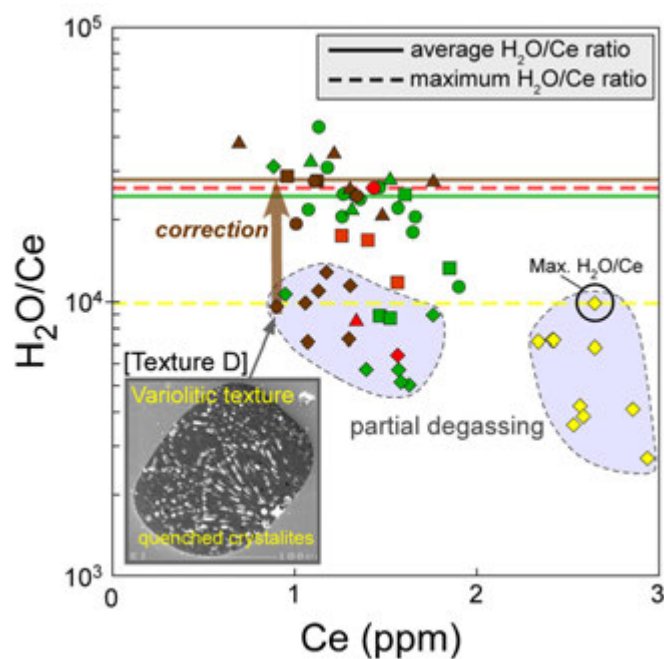


Figure DR-4.  $H_2O/Ce$  plotted against Ce of melt inclusions of high-Si-D (green) and high-Si-V (brown), and low-Si-D (red) and low-Si-F (yellow). Variolitic inclusions (solid diamonds) (Figs. 1D, DR-2D) have consistently lower  $H_2O/Ce$  ratios compared to glass in melt inclusions comprising pure glass and a few shrinkage vesicles (circles, squares and triangles) (Figs. 1A, 1B, 1C, DR-2A, 2B, 2C) of the same geochemical type. These variolitic inclusions are considered to have partly lost their water upon entrapment due to degassing. For these inclusions, the original water contents were restored based on Ce contents, by assuming the original  $H_2O/Ce$  ratios of the variolitic samples to be equal to the average  $H_2O/Ce$  ratio of undegassed samples of the same geochemical type.

Data Repository

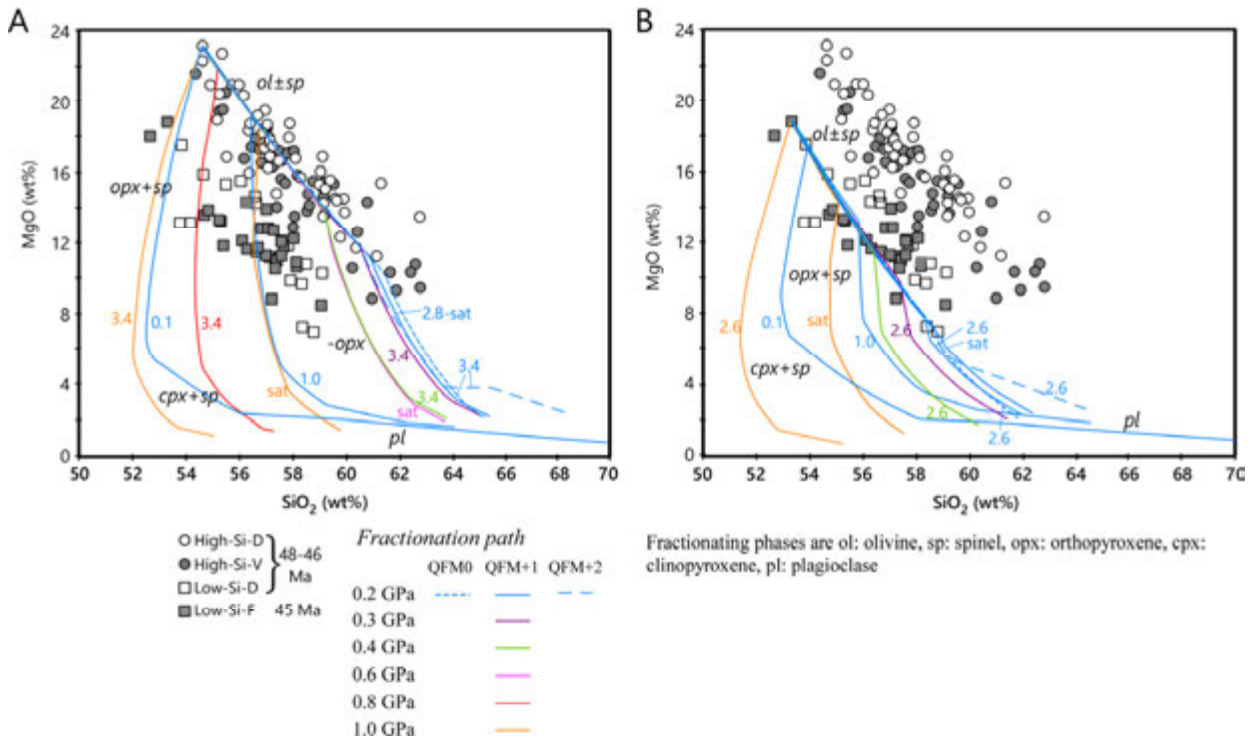


Figure DR-5. Examples of fractional crystallization paths for primary boninite magmas of the high-Si-D (A) and the low-Si-F (B) by alphaMELTS (Smith and Asimow, 2005), compared with boninitic melt inclusions (circles and squares). The numbers beside the paths are H<sub>2</sub>O contents (wt%) in the primary magmas. Calculations were done under fO<sub>2</sub> of Δlog(FMQ)=+1 at pressures 0.2-1.0 GPa, and also under fO<sub>2</sub> of Δlog(FMQ)=0 and +2 at 0.2 GPa. Change in fO<sub>2</sub> by 2 log units only slightly shifts the fractionation paths. The high-Si boninitic inclusions are mostly plot around low-P (<0.4 GPa), high-H<sub>2</sub>O (>2.8 wt%) paths. Higher pressure or lower H<sub>2</sub>O content leads to earlier crystallization of orthopyroxene and rapid decreases of MgO, away from the clusters of melt inclusion compositions. The variation of the low-Si inclusions also consistent with low-P (<0.3 GPa), high-H<sub>2</sub>O (>2.6 wt%) conditions, suggesting minimal H<sub>2</sub>O loss during fractionation. Those plotted at higher MgO than the olivine-fractionation paths suggest mixing of relatively primitive and differentiated melts.

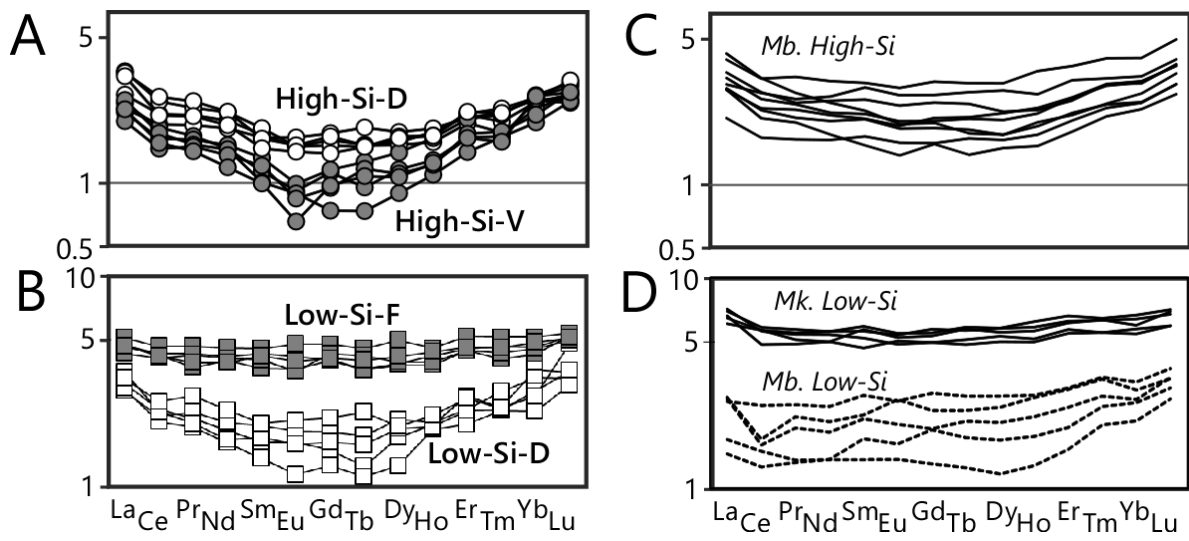


Figure DR-6. Chondrite-normalized REE patterns for the high-Si-D and high-Si-V (A) and the low-Si-D and low-Si-F (B) melt inclusions, compared with the whole-rock compositions (after Kanayama et al., 2012) of high-Si boninite from the 48-46 Ma Maruberiwan Formation (Mb.) (C), and those of low-Si boninites from the 45-Ma Mikazukiya (Mk.) and 48-46 Ma Maruberiwan (Mb.) Formation (D).





Table DR-2. Repeated analyses of standard glass NIST610, NIST612, and BIR. Reference values are from Jochum and Nohl (2008).

<b>NIST610</b>	Li	B	Sc	Ti	V	Co	Ni	Rb	Sr	Y	Zr	Nb	Cs	Ba	La	Ce	Pr	Nd	Sm	Eu	Gd	Tb	Dy	Ho	Er	Tm	Yb	Lu	Hf	Ta	Pb	Th	U	
Reference value [ $\mu\text{g/g}$ ]	485	356	441	434	442	405	444	431	497	450	440	419	361	424	457	448	430	431	451	461	420	443	427	449	426	420	462	435	418	377	413	451	457	
Average of 24 anal. [ $\mu\text{g/g}$ ]	491	250	511	502	488	445	405	454	579	584	537	506	405	489	500	519	517	500	525	508	533	549	533	558	558	528	546	551	521	532	463	528	508	
Standard deviation [ $\mu\text{g/g}$ ]	17	61	36	18	12	11	24	9	27	55	42	19.2	10.2	15.0	27.3	16.3	23.3	27.7	31.2	29.9	40.5	50.0	48.3	53.9	51.8	59.0	48.5	62.0	54.9	35.9	12.9	44.2	13.8	
RSD (%)	3.4	24.2	7.0	3.6	2.5	2.5	6.0	2.0	4.7	9.4	7.9	3.8	2.5	3.1	5.5	3.1	4.5	5.5	5.9	5.9	7.6	9.1	9.1	9.7	9.3	11.2	8.9	11.3	10.5	6.7	2.8	8.4	2.7	
Accuracy (%)	1.4	-42.5	13.7	13.6	9.4	9.0	-9.7	5.1	14.1	23.0	18.0	17.1	10.8	13.3	8.6	13.8	16.8	13.8	14.1	9.2	21.3	19.3	19.9	19.4	23.7	20.4	15.4	21.1	19.9	29.2	10.8	14.7	10.0	
<b>NIST612</b>	Li	B	Sc	Ti	V	Co	Ni	Rb	Sr	Y	Zr	Nb	Cs	Ba	La	Ce	Pr	Nd	Sm	Eu	Gd	Tb	Dy	Ho	Er	Tm	Yb	Lu	Hf	Ta	Pb	Th	U	
Reference value [ $\mu\text{g/g}$ ]	42	43	44	45	46	47	48	49	50	51	52	53	54	55	56	57	58	59	60	61	62	63	64	65	66	67	68	69	70	71	72	73	74	
Average of 9 anal. [ $\mu\text{g/g}$ ]	42	26	41	43	41	40	36	33	84	44	42	40	46	41	38	43	41	39	41	38	41	43	41	42	44	42	43	42	41	42	43	41	41	
Standard deviation [ $\mu\text{g/g}$ ]	1	2	0	1	0	0	1	0	1	1	1	0.6	0.7	0.3	0.6	0.3	0.4	0.3	0.3	0.4	0.7	0.5	0.7	1.1	1.2	0.6	0.6	0.7	0.1	0.0	0.4	0.3	0.4	
RSD (%)	2.5	6.2	1.1	2.2	0.9	0.8	3.5	1.5	0.9	2.0	2.3	1.5	1.6	0.6	1.6	0.8	1.0	0.9	0.7	1.1	1.7	1.2	1.8	2.6	2.7	1.5	1.4	1.6	0.2	0.0	0.9	0.7	1.1	
Accuracy (%)	1.0	-63.2	-5.8	-3.5	-10.2	-16.5	-31.9	-46.0	41.0	-14.3	-21.8	-31.9	-16.8	-32.2	-45.3	-32.4	-39.3	-50.2	-46.4	-60.6	-51.4	-45.6	-55.6	-51.9	-50.5	-58.8	-57.7	-62.2	-70.3	-66.7	-66.4	-77.6	-79.4	
<b>BIR-1G</b>	Li	B	Sc	Ti	V	Co	Ni	Rb	Sr	Y	Zr	Nb	Cs	Ba	La	Ce	Pr	Nd	Sm	Eu	Gd	Tb	Dy	Ho	Er	Tm	Yb	Lu	Hf	Ta	Pb	Th	U	
Reference value [ $\mu\text{g/g}$ ]	3		43	5400	326	52	178	0.2	109	14	14	0.52	0.01	6.50	0.61	1.89	0.37	2.37	1.09	0.52	1.85	0.35	2.55	0.56	1.70	0.24	1.64	0.25	0.57	0.04	3.70	0.03	0.02	
Average of 13 anal. [ $\mu\text{g/g}$ ]	3	2	41	5740	327	54	143	0	110	14	14	1	0	7	1	2	0	110	2	1	1	2	0	2	1	2	0	2	0	1	0	4	0	0
Standard deviation [ $\mu\text{g/g}$ ]	0	1	1	114	8	1	12	0	3	0	0	0	0	0	0	0	0	0	0	0	0	0	0	0	0	0	0	0	0	0	0	0	0	0
RSD (%)	3.1	53.0	2.3	2.0	2.3	2.0	8.5	5.5	2.4	3.0	2.5	6.2	71.4	3.7	4.5	3.1	4.2	4.4	3.4	3.8	4.2	6.8	5.0	6.2	3.5	5.6	5.0	9.0	8.4	27.9	3.7	16.9	30.8	
Accuracy (%)	-0.7		-4.4	5.9	0.4	4.5	-24.3	-0.3	0.8	0.2	-2.9	-1.9	-36.8	1.4	-3.3	3.8	0.3	-1.0	-0.2	0.1	-9.0	-2.9	-2.9	-5.7	-4.8	-3.2	-2.3	-7.3	-3.8	3.2	-3.4	-6.2	-37.2	